Numerical simulation and experimental validation of a direct current air corona discharge under atmospheric pressure*

Liu Xing-Hua(刘兴华)[a)†], He Wei(何 为)[a)], Yang Fan(杨 帆)[a)],
Wang Hong-Yu(王虹宇)[b)], Liao Rui-Jin(廖瑞金)[a)], and Xiao Han-Guang(肖汉光)[a)]

[a)] *State Key Laboratory of Power Transmission Equipment & System Security and New Technology, Chongqing University, Chongqing* 400044, *China*

[b)] *Department of Physics, Anshan Normal University, Anshan* 114005, *China*

(Received 6 October 2011; revised manuscript received 24 February 2012)

Air corona discharge is one of the critical problems associated with high-voltage equipment. Investigating the corona mechanism plays a key role in enhancing the electrical insulation performance. An improved self-consistent multi-component two-dimensional plasma hybrid model is presented for the simulation of a direct current atmospheric pressure corona discharge in air. The model is based on plasma hydrodynamic and chemical models, and includes 12 species and 26 reactions. In addition, the photoionization effect is introduced into the model. The simulation on a bar-plate electrode configuration with an inter-electrode gap of 5.0 mm is carried out. The discharge voltage–current characteristics and the current density distribution predicted by the hybrid model agree with the experimental measurements. In addition, the dynamics of volume charged species generation, discharge current waveform, current density distribution at an electrode, charge density, electron temperature, and electric field variations are investigated in detail based on the model. The results indicate that the model can contribute valuable insights into the physics of an air plasma discharge.

Keywords: corona discharge, hybrid model, discharge voltage–current characteristics, current density distribution

PACS: 52.25.Dg, 52.65.–y, 52.80.Hc, 52.40.Kh **DOI:** 10.1088/1674-1056/21/7/075201

1. Introduction

Due to the tremendous increase in demand for power transmitted over long distances, many direct current (DC) transmission lines have been built in China. High-voltage equipment is the backbone of modern power systems. Safe transmission lines are determined by the reliability of the electrical insulation system, which is of primary importance. Along with the development of extra and ultra high-voltage transmission lines, the air corona discharge has become a problem associated with the high-voltage lines. Air corona discharge on DC transmission lines can lead to the deterioration of insulation systems and power loss. Hence, it has drawn an increasing amount of attention. In addition, air corona discharge also occurs in high-voltage industrial, scientific, and engineering applications, and it plays a critical role in the insulation performance of such applications. High-voltage insulator system behaviors can be predicted using detailed knowledge of the fundamental corona discharge generation mechanisms.[1] Therefore, investigating the corona mechanism plays a key role in enhancing the electrical insulation system.

Despite those recent improvements, the physical mechanism associated with the dynamics of corona discharge is still unclear. One option which may be used to investigate the corona discharge in detail is numerical modeling. Nahomy,[2] who adopted 430 chemistry reactions in an air discharge, presented one of the most comprehensive compilations of chemistry mechanisms. The mathematical modeling of DC or an impulse discharge was utilized to understand the physical mechanism and the chemical processes evolved after

*Project supported by the National Basic Research Program of China (Grant No. 2011CB209401), the National Natural Science Foundation of China (Grant No. 51007096), and the Scientific Research Foundation of State Key Lab of Power Transmission Equipment and System Security, China (Grant No. 2007DA10512709102).

†Corresponding author. E-mail: hua101334@gmail.com

© 2012 Chinese Physical Society and IOP Publishing Ltd

the above milestone paper. Macheret *et al.*[3] demonstrated air plasma generation through repetitive high-voltage nanosecond pulses. Salasoo *et al.*[4] investigated the ion densities and the electric field distribution by simulating the corona discharge in a pipe type precipitator. Pancheshnyi *et al.*[5] developed a reduced air model with 10 species based on the mechanism of Nahomy to simulate the streamer discharge at a pressure of 1 atm. Popov presented a plasma model of fast heating of a nitrogen–oxygen mixture excited by the gas discharge. They calculated the contribution of different processes to fast gas heating. Morrow[6] investigated the corona discharge in oxygen and other gases using the finite-element method. Kumara *et al.*[7] presented a two-dimensional model to examine the positive impulse corona on polymeric surfaces and found that the resulting radius of the charged area was smaller than the glow corona. Gordiets[8] developed a reduced air chemistry model to investigate the role of excited neutral molecules and atoms in the air discharge. Recently, Liang *et al.*[9] investigated the influence of a reduced electric field on the evolvement characteristics of plasma for a N_2/O_2 discharge. Jiang *et al.*[10] carried out experimental studies under atmospheric pressure of a He plasma jet. Cai *et al.*[11] studied outgassing in the breakdown of the dielectric surface irradiated by a high power microwave. Yin *et al.*[12] simulated the reaction diffusion process of air plasma in an open atmospheric environment.

In this paper, a self-consistent, multi-component, and two-dimensional plasma hybrid model is developed to simulate the atmospheric pressure DC corona discharge in air, which is based on plasma hydrodynamics and the chemical model. The important feature of the hybrid model is that it introduces the photoionization effect, the electron energy conservation equation, the momentum balance equation and considers more comprehensive species and chemical reactions. Moreover, it differs from the previous work in the formulation of electron energy boundary conditions. The aim of this work is to report the details of the developed plasma hybrid model, evaluate the validity of the simulation against experimental data available in the literature, and to understand the electrical and the physical characteristics of the air plasma corona discharge.

In the following section, detailed descriptions are presented for the air discharge mathematical model and the plasma chemistry mechanism. The corresponding results and discussion are given in Section 3, and the conclusion is given in Section 4.

2. Model of corona discharge in air

The air corona discharge is described using the coupled electron conservation equation, the electron energy conservation equation, the heavy species multi-component diffusion transport equation, the momentum balance equation, and Poisson's equation for electric potential.

2.1. Governing equations

Electron conservation is described by the electron density continuity equation[13]

$$\frac{\partial n_{\mathrm{e}}}{\partial t} + \boldsymbol{\nabla} \cdot (-(\mu_{\mathrm{e}} \cdot \boldsymbol{\nabla}\phi) n_{\mathrm{e}} - D_{\mathrm{e}} \boldsymbol{\nabla} n_{\mathrm{e}}) = R_{\mathrm{e}}, \quad (1)$$

$$\begin{aligned} R_{\mathrm{e}} = {} & \alpha n_{\mathrm{e}} \left| w_{\mathrm{e}} \right| - \eta n_{\mathrm{e}} \left| w_{\mathrm{e}} \right| - R_{\mathrm{ei}} n_{\mathrm{e}} n_{\mathrm{p}} \\ & + v_{\mathrm{det}} n_{\mathrm{n}} + S_{\mathrm{ph}} + S_0, \end{aligned} \quad (2)$$

where n_{e}, n_{p}, and n_{n} denotes the number density of the electron, positive ion, and negative ion, respectively; φ is the electric potential; μ_{e} is the electron mobility; D_{e} is the electron diffusion coefficient; R_{e} is the net rate of electron production due to the chemical reactions; w_{e} is the drift velocity of the electron; α is the ionization coefficient; η is the net attachment coefficient; R_{ei} is the coefficient of electron–ion recombination; v_{det} is the detachment coefficient; and $S_0 = 10^7\ \mathrm{m^{-3} \cdot s^{-1}}$ is the rate of appearance of electrons due to the background ionization. S_{ph} is the rate of photoionization calculated by the following equation:[14]

$$S_{\mathrm{ph}} = \frac{1}{4\pi} \frac{P_{\mathrm{q}}}{p + P_{\mathrm{q}}} \int_V \mathrm{d}^3 r_1 \frac{S_{\mathrm{ion}}(\boldsymbol{r}_1)}{|\boldsymbol{r} - \boldsymbol{r}_1|^2} \Psi(|\boldsymbol{r} - \boldsymbol{r}_1| \cdot p), \quad (3)$$

where $1/4\pi$ is the normalization constant; p is the gas pressure; P_{q} is the quenched pressure of excited state nitrogen atoms and is set at 30 torr for air; $S_{\mathrm{ion}}(\boldsymbol{r}_1)$ is the rate of ionization; $\Psi(|\boldsymbol{r} - \boldsymbol{r}_1| \cdot p)$ is the coefficient of absorption of the ionizing radiation; and $\boldsymbol{r}$ is the distance between the points of radiation and absorption of photon. The integral in Eq. (3) is approximated by two Helmholtz differential equations which can be much more efficiently solved than the integral.

In order to accurately describe the sheath region in the corona discharge under atmospheric pressure, the electron temperature is included in the model.

The complete equation for electron energy conservation is[15]

$$\frac{3}{2}\frac{\partial(k_{\rm B}n_{\rm e}T_{\rm e})}{\partial t}+\boldsymbol{\nabla}\left(\frac{5}{2}k_{\rm B}T_{\rm e}\boldsymbol{\Gamma}_{\rm e}-\frac{5}{2}k_{\rm B}n_{\rm e}D_{\rm e}\boldsymbol{\nabla}T_{\rm e}\right)$$
$$=\boldsymbol{j_e}\cdot\boldsymbol{E}-n_{\rm e}\sum_k n_k\eta_k-2n_{\rm e}k_{\rm B}\frac{m_{\rm e}}{M_k}(T_{\rm e}-T)v_{\rm e,n}, \quad (4)$$

where $T_{\rm e}$ is the electron temperature; $\boldsymbol{\Gamma}_{\rm e}$ is the electron flux; n_k is the number density of species k; η_k is the rate coefficient of energy loss for the collision of electrons with species k; $m_{\rm e}$ is the mass of the electron; M_k is the mass of species k; and $v_{\rm e,n}$ is the electron momentum transfer collision frequency. The right-hand side of Eq. (4) is the source terms, $\boldsymbol{j}_{\rm e}\cdot\boldsymbol{E}$ represents the energy gain due to the electron Joule heating, and the last two terms represent the energy losses due to non-elastic and elastic collisions respectively. T is the gas temperature, which can be obtained by solving an independent gas energy equation. However, for the low-pressure discharge and in the absence of flow, a fixed gas temperature is adopted in the present work.

For the heavy species (i.e., positive ions, negative ions, and neutral species), the multi-component conservation equation used in the corona discharge is given by[16]

$$\frac{\partial n_k}{\partial t}+(\boldsymbol{u}\cdot\boldsymbol{\nabla})n_k=\boldsymbol{\nabla}\cdot\boldsymbol{j}_k+R_k+S_{\rm ph}, \quad (5)$$

where $\boldsymbol{u}$ is the mass averaged hydrodynamic velocity vector; R_k represents the rate of change of species k due to the chemical kinetics; and $\boldsymbol{j}_k$ is the diffusive flux vector defined as

$$\boldsymbol{j}_k=D_k\boldsymbol{\nabla}n_k-Z_k\mu_k n_k\boldsymbol{\nabla}\varphi-S_k, \quad (6)$$

with D_k being the diffusion coefficient, Z_k the electric charge, and μ_k the mobility for species k. The expression for S_k is[17]

$$\boldsymbol{S}_k=nD_k^T\frac{\boldsymbol{\nabla}T}{T}+n_kD_k\frac{\boldsymbol{\nabla}M}{M}+n_k\sum_j D_j\boldsymbol{\nabla}w_j$$
$$-n_k\frac{\boldsymbol{\nabla}M}{M}\sum_j D_j\boldsymbol{\nabla}w_j-n_k\frac{\boldsymbol{\nabla}T}{T}\sum_j D_j^T, \quad (7)$$

where n is the total density; D_k^T is the multi-component thermal diffusion coefficient; M is the mole averaged molecular weight; and w_j is the mass fraction of species j.

The momentum equation for the heavy species can be written as[18]

$$\frac{\partial n\boldsymbol{u}}{\partial t}+\boldsymbol{\nabla}\cdot(n\boldsymbol{u}\boldsymbol{u})=-\boldsymbol{\nabla}p+\mu\nabla^2\boldsymbol{u}$$
$$+\frac{\mu}{3}\boldsymbol{\nabla}(\boldsymbol{\nabla}\boldsymbol{u})+\sum_k n_k\boldsymbol{F}_k, \quad (8)$$

where μ is the dynamic viscosity; and $\boldsymbol{F}_k$ is the body force term action on species k.

Finally, the electric field can be calculated according to the Poisson equation

$$\boldsymbol{\nabla}\cdot(\varepsilon_0\boldsymbol{\nabla}\varphi)=-e(n_{\rm p}-n_{\rm e}-n_{\rm n}), \quad (9)$$
$$\boldsymbol{E}=-\boldsymbol{\nabla}\varphi, \quad (10)$$

where ε_0 is the vacuum permittivity.

2.2. Boundary conditions

An essential part of the model are the boundary conditions used in the computational process. The flux boundary condition is imposed for all species densities at the electrodes, and the electron fluxes at the cathode and the anode are

$$\boldsymbol{\Gamma}_{\rm e}=\frac{1}{4}v_{\rm th,e}n_{\rm e}-\gamma\sum_i q_i\boldsymbol{\Gamma}_i, \quad (11)$$
$$v_{\rm th,e}=\left(\frac{8k_{\rm B}T_{\rm e}}{\pi m_{\rm e}}\right)^{1/2}, \quad (12)$$

where $\boldsymbol{\Gamma}_{\rm e}$ and $\boldsymbol{\Gamma}_i$ are the electron density flux and the ion density flux, respectively; $v_{\rm th,e}$ is the electron thermal velocity; and γ is the secondary electron emission coefficient.

The boundary condition for electron energy is expressed as

$$\frac{5}{2}k_{\rm B}T_{\rm e}\boldsymbol{\Gamma}_{\rm e}-\frac{5}{2}n_{\rm e}k_{\rm B}D_{\rm e}\nabla T_{\rm e}$$
$$=\frac{5}{2}k_{\rm B}T_{\rm e}\left[\frac{1}{4}n_{\rm e}v_{\rm th,e}+(a-1)\mu_{\rm e}n_{\rm e}\right]$$
$$-a\left(\frac{5}{2}k_{\rm B}T_{\rm se}\right)\gamma\boldsymbol{\Gamma}_i, \quad (13)$$

where $T_{\rm se}$ is the temperature of the second electron ejected from the electrode ($T_{\rm se}\approx 5$ eV); $a=0$ if the electric field is directed away from the electrode, and $a=1$ if the electric field is directed toward the electrode.

The corresponding boundary condition for the ions is given by

$$\boldsymbol{\Gamma}_i=\frac{1}{4}v_{{\rm th},i}n_i+a\mu_i\boldsymbol{E}n_i, \quad (14)$$
$$v_{{\rm th},i}=\left(\frac{8k_{\rm B}T}{\pi m_i}\right)^{1/2}, \quad (15)$$

and for the neutral species, it is

$$\boldsymbol{\Gamma}_{\rm s}=\frac{1}{4}v_{\rm th,s}n_{\rm s}, \quad (16)$$

$$v_{\mathrm{th,s}} = \left(\frac{8k_{\mathrm{B}}T}{\pi m_{\mathrm{s}}}\right)^{1/2}, \tag{17}$$

where $v_{\mathrm{th},i}$ and $v_{\mathrm{th,s}}$ are the ion and the neutral species thermal velocities at the electrode, respectively.

The charged ions are quenched to the neutral species due to the surface reactions

$$\begin{aligned} &\mathrm{N_2^+ \rightarrow N_2}, \quad \mathrm{N_4^+ \rightarrow 2N_2}, \quad \mathrm{O_2^+ \rightarrow O_2}, \\ &\mathrm{O_4^+ \rightarrow 2O_2}, \quad \mathrm{O_2^+N_2 \rightarrow N_2 + O_2}, \\ &\mathrm{O_2^- \rightarrow O_2}, \quad \mathrm{O^- \rightarrow 0.5O_2}. \end{aligned} \tag{18}$$

At the electrode surfaces, neutral oxygen atoms are quenched to the oxygen molecules by the surface reaction

$$\mathrm{O \rightarrow 0.5O_2}. \tag{19}$$

The boundary condition of the electric potential is specified to be $V = 0$ at the plate electrode, and $V = V_0$ at the driven bar electrode. All the heavy species temperatures at the electrode are assumed to be at air temperature. Finally, the homogeneous Neumann conditions for the particle species densities and the potential are adopted on the symmetry axis.

2.3. Air chemistry and transport

In the plasma-chemistry model 12 species (e, O, O_2, O_3, N_2^+, N_4^+, O_2^+, O_4^+, $O_2^+N_2$, O_2^-, O^-, and N_2) are considered. A total of 26 reactions are considered, which include elastic scattering, ionization, two-body recombination, three-body recombination, dissociative recombination, molecular ion conversion, excitation, de-excitation, and so on. Table 1 lists the reaction processes that are taken into account in the model.

Table 1. Important reaction processes in air corona discharge.

Number	Reaction	Rate coefficient	ΔE/eV
R_1	O_2+e→e+O_2	$f(\varepsilon)$	1.0
R_2	N_2+e→e+N_2	$f(\varepsilon)$	1.0
R_3	O_2+e→2e+O_2^+	$f(\varepsilon)$	12.06
R_4	N_2+e→2e+N_2^+	$f(\varepsilon)$	15.6
R_5	N_2^++N_2+M →N_4^++M	5×10^{-41}	
R_6	N_4^++O_2 →O_2^++2N_2	2.5×10^{-16}	
R_7	N_2^++O_2 →O_2^++N_2	$1.04\times10^{-15}T^{-0.5}$	
R_8	2N_2+O_2^+ →$O_2^+N_2$+N_2	$8.1\times10^{-38}T^{-2}$	
R_9	$O_2^+N_2$+N_2 →O_2^++2N_2	$14.6T^{-5.3}\exp(-2357/T)$	
R_{10}	$O_2^+N_2$+O_2 →O_4^++N_2	1×10^{-15}	
R_{11}	O_2^++O_2+M →O_4^++M	$2.04\times10^{-34}T^{-3.2}$	
R_{12}	O_4^++e→2O_2	$1.4\times10^{-12}\left(300/T_{\mathrm{e}}\right)^{0.5}$	
R_{13}	O_2^++e→2O	$2.42\times10^{-13}\left(300/T_{\mathrm{e}}\right)$	
R_{14}	2O_2+e→ O_2+O_2^-	$2\times10^{-41}\left(300/T_{\mathrm{e}}\right)$	
R_{15}	O_4^++O_2^- → 3O_2	1×10^{-13}	
R_{16}	O_4^++O_2^-+M →3O_2+M	2×10^{-37}	
R_{17}	O_2^++O_2^-+M →2O_2+M	2×10^{-37}	
R_{18}	O+O_2+M →O_3+M	2.5×10^{-46}	
R_{19}	2e + N_2^+ → N_2+ e	$5.651\times10^{-27}T_{\mathrm{e}}^{-0.8}$	
R_{20}	e + N_2^+ + N_2 → 2N_2	$6.07\times10^{-34}T_{\mathrm{e}}^{-2.5}$	
R_{21}	O_2+ e → O + O^-		3.6

Note: two-body reactions have units of $\mathrm{m^3{\cdot}s^{-1}}$; three-body rates are have units of $\mathrm{m^6{\cdot}s^{-1}}$, T_{e} and T in the unit of K, and M=O_2, N_2.

2.4. Computational implementation

The bar-plate electrode system model is simplified into a two-dimensional representation using the rotational symmetry. There are two electrodes that separate from each other with a gap of $L = 5$ mm, the plate electrode is grounded, and the bar electrode is driven with DC voltage V_0. In this paper, the pressure of air discharge is fixed at 1 atm, and the gas temperature is assumed to be a constant (300 K). Figure 1 shows the computational domain. The numerical model is implemented in COMSOL Multiphysics based on the finite-element method. To speed up the convergence, some appropriate initial conditions and a time-dependent solver provided in the software are

adopted and utilized first, then the stationary nonlinear solver Direct (UMFPACK) is started when the solution is already steady. To resolve the steep layers near the electrodes, a mesh adaptation is used. The numerical convergence is checked by performing a successive refinement of the space grid. The iteration process is stopped when the relative error is smaller than 10^{-4}.

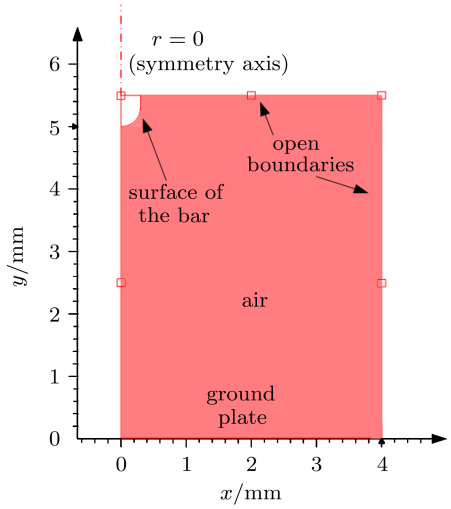


Fig. 1. (colour online) Computational domain.

3. Results and discussion

The developed model is verified by comparing the computational discharge voltage–current (V–I) characteristics and current density with the experimental results available in Ref. [19].

Figure 2 shows the comparison between the computational and the corresponding experimental results for DC air corona discharge under atmospheric pressure. The discharge voltage–current curve shows a gradual decrease in slope with the increasing current. The computational data shows good agreement with the experimental data, particularly at the low discharge voltage. However, there is a slight discrepancy between the computational and experimental data in the higher discharge voltage region. The adopted simple chemistry mechanism and the secondary electron emission coefficient on the ion impact energy in the model are possibly responsible for this discrepancy. The comparison between the computational and experimental discharge voltage–current characteristics shows that they are exactly the same, which confirms the validity of the model.

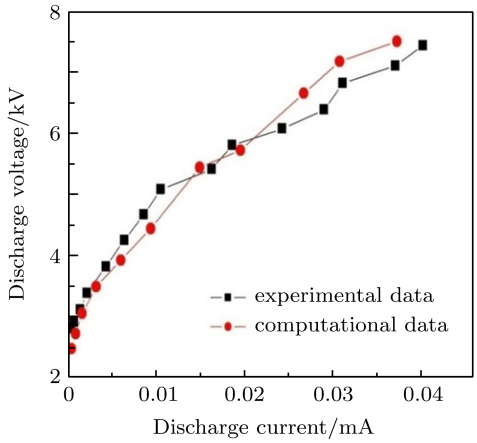


Fig. 2. (colour online) A comparison of the discharge voltage–current (V–I) characteristics between the computational and experimental data. The pressure and the interelectrode gap are fixed at 1 atm and 5 mm, respectively.

Figure 3 shows the comparison between the computational and the experimental current densities available in the literature across the interelectrode gap. An excellent agreement between the computational and experimental data is obtained. Therefore, the developed model is also verified by comparing the computational current density with the experimental results. The current density in the negative corona is estimated to be around 10^5 A/m^2, which is in the order of that of the negative glow of the DC glow discharge in air.[20] The current density in the diffuse glow near the anode is about three orders of magnitude lower, and it can be used to estimate the electron density and the charged ion densities, which are required to explain the diffuse glow phenomenon.

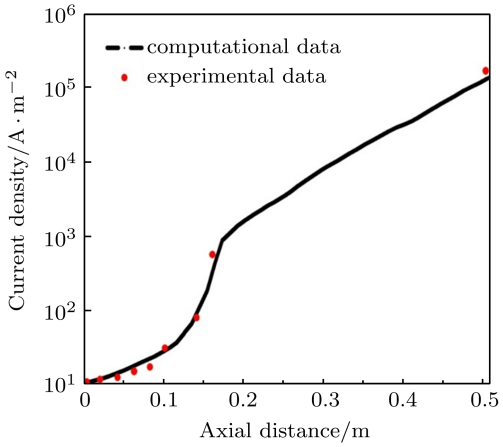


Fig. 3. (colour online) The current density across the interelectrode gap in air obtained from the experiment and the model. Pressure $p = 1$ atm, applied voltage $V = -6000$ V.

Figure 4(a) demonstrates that the current density at the anode increases as time progresses, and

the maximum value occurs at a radial distance of 1.1×10^{-4} m. This is owing to the maximum net negative charge density, and is also where the higher number of free electrons exist. The current density adjacent to the symmetry axis is shown to increase continuously and to expand radically outwards with the anode sheath region covering a greater surface area of the anode. This is because the rate of electron absorption into the anode depends on the electrical field, which is larger at the symmetry axis and reduces as it moves radially outwards along the anode. Figure 4(b) shows the discharge current waveform in the electrode gap. The pulse of the discharge current is characterized by a fast rising front and a slower decay. Some oscillations are found on the decaying curve. The maximum discharge current is just above 2.3×10^{-5} A. The initial pulse width is around 6 ns, and the tail lasts approximately 50 ns. The long tail discharge current waveform may stem from the artificial numerical diffusion.

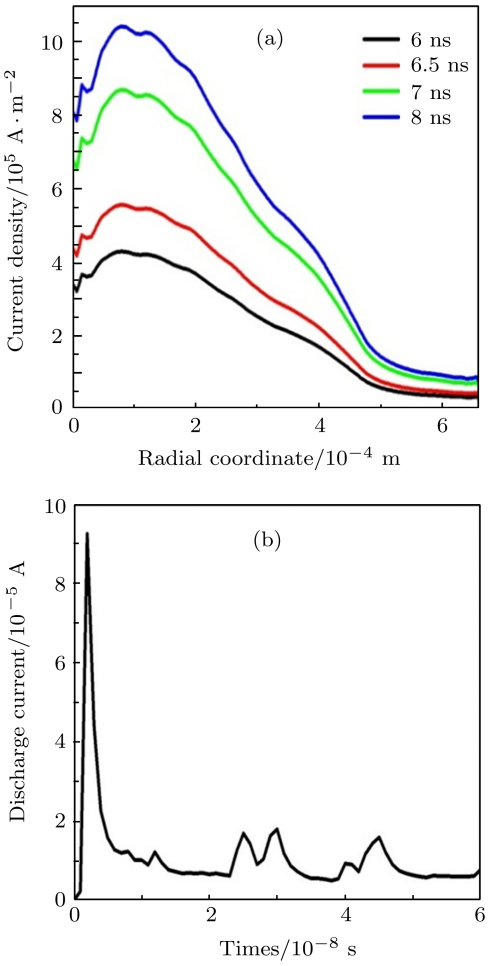


Fig. 4. (colour online) (a) The current density distributions along the anode at different time. (b) The discharge current waveform in the electrode gap. Pressure $p = 1$ atm, applied voltage $V = 6000$ V.

Figure 5 shows the charge densities along the symmetry axis at three different times. The charge density within the bulk plasma remains a constant and abruptly increases close to the electrode surface as time progresses. In addition, the charge clouds in the space move toward the cathode due to the higher electric field as time progresses. The rate of increase of the charge density at the cathode is much greater than that at the anode. This is owing to the higher ionization rate as a result of the higher electric field. In the vicinity of the anode, the positive ion density is higher than the sum of the negative ion density and the electron density resulting in a net positive space charge. Consequently, the anode sheath electrical field points away from the anode, resulting in an inverted anode sheath as shown in Fig. 10.

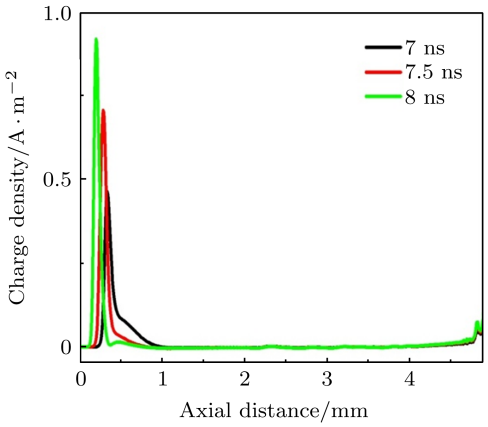


Fig. 5. (colour online) Charge density distributions along the symmetry axis at three different times. Pressure $p = 1$ atm, applied voltage $V = 6000$ V.

Figure 6 shows the electron densities at four different times along the axis. A large number of electrons accumulated in the anode sheath region. At time $t = 6$ ns, the electron density is at maximum in the anode sheath region and reduces to about zero in the cathode sheath region. At time $t = 6.5$ ns, in the cathode sheath region, the electron density becomes larger than that at time $t = 6$ ns due to the secondary electron emission at the cathode surface affected by the multiplication electrons. As the primary electron avalanche builds up toward the anode, the excitation and ionization reactions also occur at the same time. At time $t = 7$ ns, the electron density increases even faster, especially in the cathode sheath region. An important feature of this reaction is that the electron density column increases in the cathode sheath as time progresses, which is caused by the effect of secondary electron emission and the ionization dominant in the

cathode sheath due to the high electric field. The electron density is observed to be in the order of 10^{20} m^{-3}, and its spatial variation is quite similar to that in the previous literature.[21]

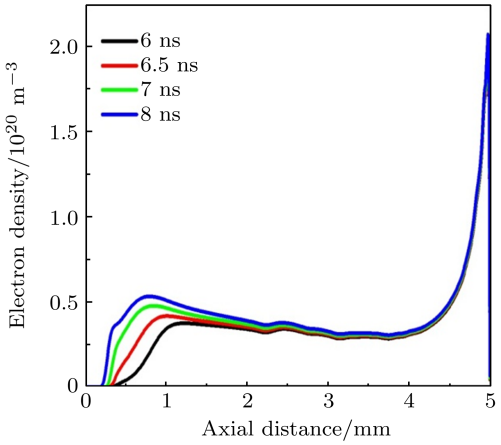


Fig. 6. (colour online) Electron densities at different time points along the axis. Pressure $p = 1$ atm, applied voltage $V = 6000$ V.

Figure 7 demonstrates the plots of positive and negative ion densities along the axis. Similarly to the electron density, the positive ion density follows the same pattern. Close to the anode in the anode sheath region, the positive ion density increases sharply to its maximum value owing to the accumulation of positive charge there. In the cathode sheath region, the positive ion density increases slightly, because the ionization collision caused by the emitted electrons from the cathode produces slow positive ions trying to escape from the cathode. It is interesting to note that the negative ion density almost maintains a uniform value in the bulk plasma compared with the distributions of the electron and positive ion density, which is caused by the fact that the attached reaction of an electron to the neutral species is almost equal to the recombination reaction of positive and negative ions.

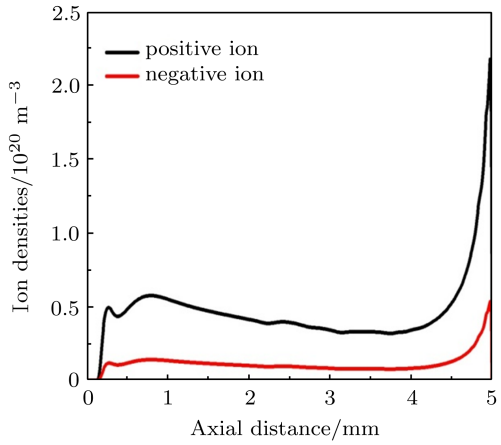


Fig. 7. (colour online) Positive and negative ion densities along the axis. Pressure $p = 1$ atm, applied voltage $V = 6000$ V.

Figure 8 shows the charged species density profiles along the axis of the air discharge. Figure 8(a) illustrates that the positive ions O_2^+ and N_2^+ are dominant compared to the other charged heavy species. In the anode sheath region, N_2^+ and O_2^+ sharply increase to the maximum value. In the cathode sheath region, O_2^+ increases to a high value, whereas the increase of N_2^+ is significant but less important, because the ionization of O_2 is relatively high compared to the ionization reaction of N_2 at the relatively high electron temperature observed in the cathode sheath region.[22] As a consequence of the dominance of O_2^+ in the cathode sheath region, the air plasma hybrid model is most sensitive to the secondary electron emission coefficient of O_2^+. The N_4^+ and O_4^+ are significantly lower than the dominant positive ions O_2^+ and N_2^+, which are generated

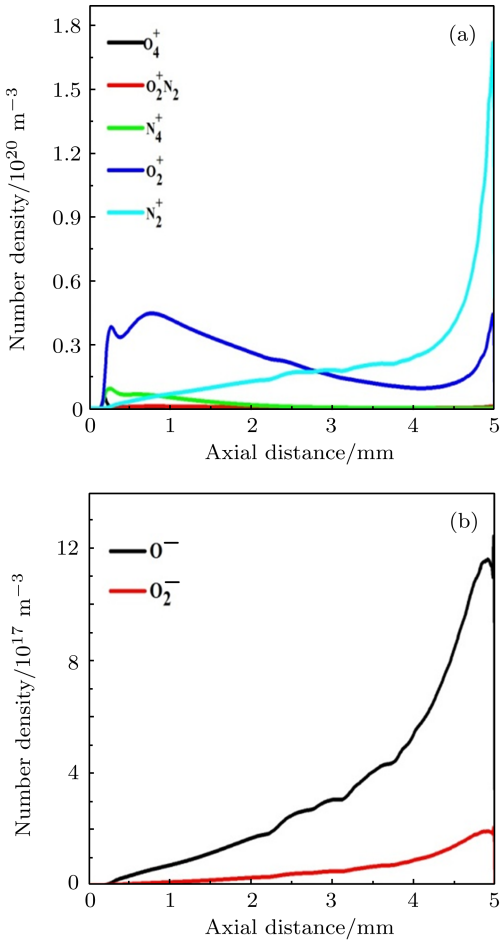


Fig. 8. (colour online) Number densities of (a) positive and (b) negative irons along the axis. Pressure $p = 1$ atm, applied voltage $V = 6000$ V.

through a three-body reaction R_5 and reactions R_{10}, R_{11}, respectively. The minimum type of positive ion is $O_2^+N_2$, which is produced through a three-body reaction R_8 and is negligible compared to the other ionized species in the air discharge. In Fig. 8(b), O^- is about one order of magnitude more than O_2, because O^- is generated by the dissociative attachment reaction R_{21}, while O_2^- is generated by the three-body reaction R_{14}. However, at higher pressure, the O_2^- density can become much higher than the O^- density.[23]

The electron temperature in the air corona discharge is extremely important. Figure 9 indicates the electron temperature distributions at different time points along the axis of the air discharge. The maximum electron temperature moves toward the cathode and increases as time progresses in the cathode sheath region. At time $t = 8$ ns, the maximum electron temperature is 7.9 eV, which is consistent with that obtained by Sigmond.[24] In the high electric field, the high electron temperature at the end of the cathode is the result of Joule heating, which leads to the production of energetic electrons in the cathode sheath region.[25,26] The electron temperature decreases to a much smaller value and keeps relative uniform electron energy in the bulk plasma, this is caused by the electron energy loss incurred from the collision reactions of the electrons with neutral species. The spatial variation of the electron temperature mirrors that of the collision ionization reaction coefficient as well as the speed of the energy transfer. Both suggest that the secondary electrons are rapidly accelerated in the cathode fall region and the space charge distorts the electron field. Thus, the electron temperature in the cathode sheath region is strengthened.

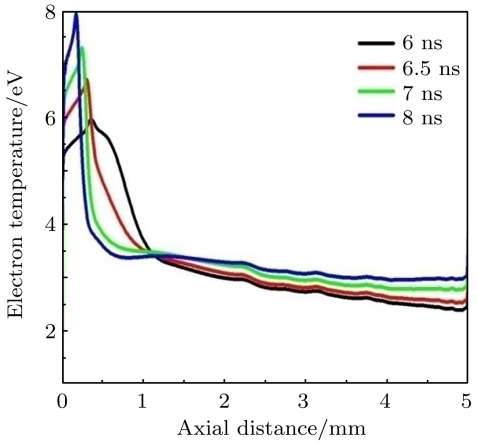


Fig. 9. (colour online) The electron temperature distributions at different time points along the axis of air discharge. Pressure $p = 1$ atm, applied voltage $V = 1000$ V.

Figure 10 demonstrates the profiles of electric potential and electric field along the axis. The electric potential decreases rapidly at about 4191.46 V in the cathode sheath. The maximum voltage drop starts at 1.2×10^{-3} m away from the cathode with the initiation of the sheath formation, and decreases almost linearly to zero. Such a profile is similar to the spectroscopic measurement for the DC plasma discharge.[27] The high electric field diminishes almost linearly to a very low value (6.8×10^5 V/m) and keeps this low level throughout the bulk plasma with a slight decrease near the anode. The phenomenon can be explained by the fact that the electric field is distorted by a large number of electrons produced through the secondary electron emission at the cathode surface. Under these conditions, a low electric field is necessary in the bulk plasma to prevent the electron flux and maintain the plasma quasi-neutrality. Therefore, the anode sheath extracts electrons and negative ions from the bulk plasma to prevent the positive ion flux keeping a high potential at the anode.[28]

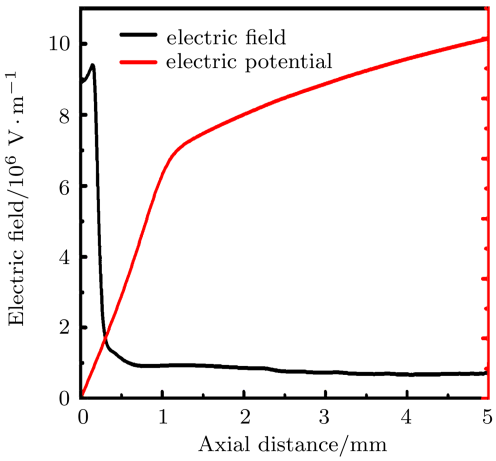


Fig. 10. (colour online) Electric potential and electric field along the axis. Pressure $p = 1$ atm, applied voltage $V = 6000$ V.

The electric field is important in the air corona discharge. Figure 11 illustrates the evolution of a two-dimensional electric field. The maximum electric field (4.16×10^6 V/m) occurs at 1.4×10^{-3} m away from the cathode in Fig. 11(a). Figure 11(b) indicates that the electric field at 6.5 ns is minimally changed compared with that at 6 ns. Figure 11(c) shows that the electric field increases to 6.8×10^6 V/m and approaches the cathode at 7 ns. Figure 11(d) describes that the electric field reaches 9.4×10^6 V/m, and extends radially to a distance of 0.6×10^{-3} m. The thickness of the cathode fall is about 0.2×10^{-3} m. As time progresses,

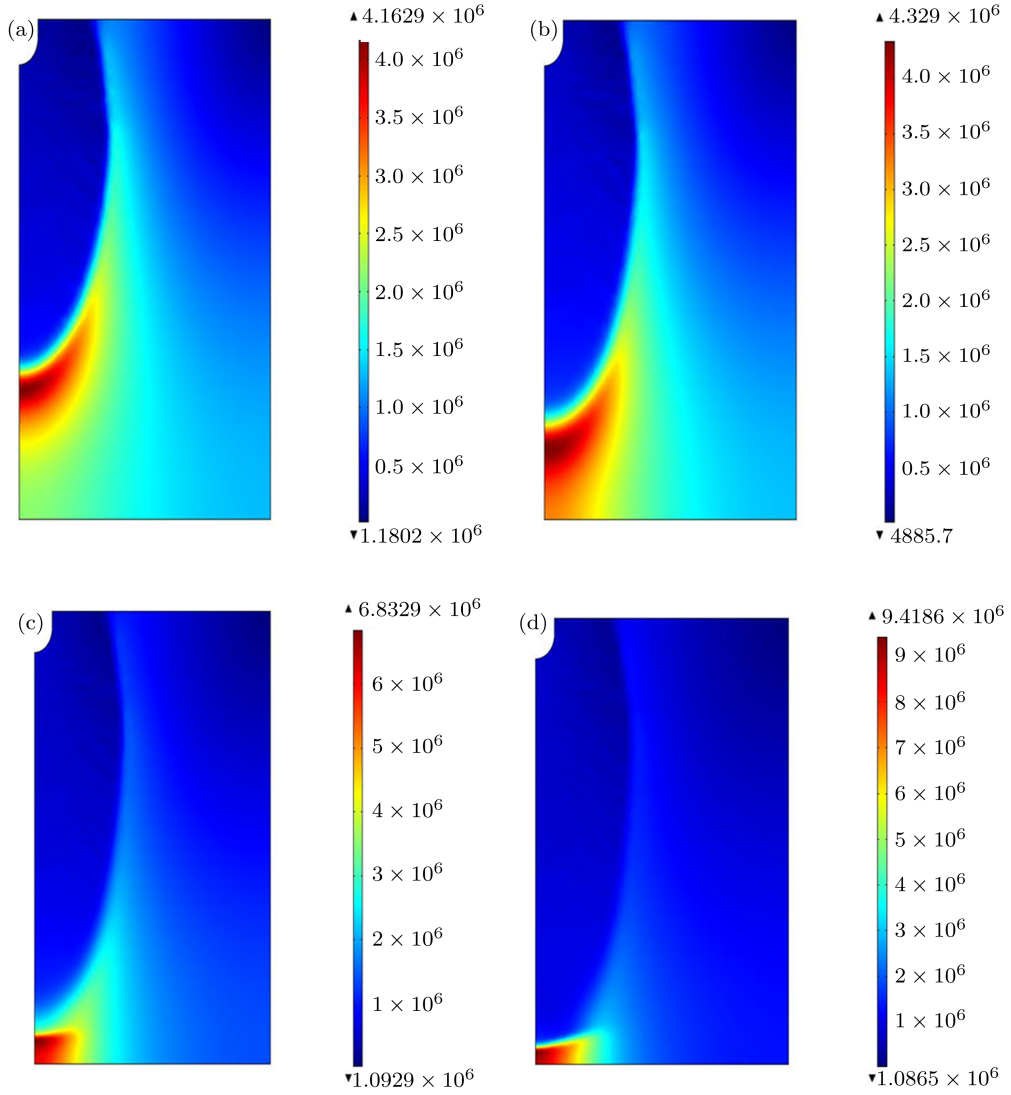


Fig. 11. (colour online) Distributions of electric field at (a) 6 ns, (b) 6.5 ns, (c) 7 ns, and (d) 8 ns, (the unit of electric field is V/m). Ressure $p = 1$ atm, applied voltage $V = 6000$ V.

the electric field increases and extends along the cathode surface, while the cathode fall shrinks in thickness. In addition, figure 11 clearly describes a very small electric field being maintained in the bulk plasma and the narrow cathode sheath.

4. Conclusions

In this paper, the numerical simulation of DC air discharge under atmospheric pressure is performed using an axisymmetric hybrid model, which introduces the photoionization effect. The model adopted for multi-dimensional applications with 12 species and 26 reactions is presented and validated using the experimental data available in the literature. This study concerns both the actual industrial application and the basic physics research. The discharge voltage–current characteristics and the current density distribution predicted by the model are found to be in good agreement with the experimental results. For the atmospheric pressure air corona discharge, the pulse of the discharge current is characterized by a fast rising front and a slower decaying curve, which includes some oscillations. The charge density within the bulk plasma is shown to remain a constant and abruptly increases close to the electrode surface as time progresses. In addition, the charge clouds in the space move toward the cathode due to the higher electric field as time progresses. O_2^+ and N_2^+ are the dominant positive ions. In addition, the number densities of O^- and O_2^- are much smaller than that of the electrons. The minimum positive ion is $O_2^+N_2$. The maximum electron temperature that arises in the cathode sheath

is caused by Joule heating in the high electric field. As time progresses, the electric field increases and extends along the cathode surface, while the cathode fall shrinks after the corona discharge hits the cathode. The presented plasma hybrid model can contribute to further understanding of the main physical mechanisms and characteristics of the atmospheric pressure air corona discharge and suggest ways to enhance the electrical insulation performance associated with the high-voltage equipment.

References

[1] Pokryvailo A, Yankelevich Y, Nissim N, Baksht R and Ashkenazy J 2006 *IEEE Trans. Plasma Sci.* **34** 104

[2] Nahomy J, Ferreira C M, Gordiets B, Pagnon D, Touzeau M and Vialle M 1995 *J. Phys.* D: *Appl. Phys.* **28** 738

[3] Macheret S O, Shneider M N and Miles R B 2002 *IEEE Trans. Plasma Sci.* **30** 1301

[4] Salasoo L, Nelson J K, Schwabe R J and Snaddon R W L 1985 *J. Appl. Phys.* **58** 2949

[5] Pancheshnyi S V and Starikovskii A Y 2003 *J. Phys.* D: *Appl. Phys.* **36** 2683

[6] Morrow R 1997 *J. Phys.* D: *Appl. Phys.* **30** 3099

[7] Kumara S, Serdyuk Y V and Gubanski S M 2009 *IEEE Trans. Dielect. El. In.* **16** 726

[8] Gordiets B F, Ferreira C M, Guerra V L, Loureiro J M A H, Nahomy J, Pagnon D, Touzeau M and Vialle M 1995 *IEEE Trans. Plasma Sci.* **23** 750

[9] Du H L, He L M, Lan Y D and Wang F 2011 *Acta Phys. Sin.* **11** 115201 (in Chinese)

[10] Jiang N and Cao Z X 2010 *Acta Phys. Sin.* **59** 3324 (in Chinese)

[11] Cai L B and Wang J G 2011 *Acta Phys. Sin.* **60** 025217 (in Chinese)

[12] Yin Z Q, Zhao P P, Dong L F and Fang T Z 2011 *Acta Phys. Sin.* **60** 025206 (in Chinese)

[13] Hagelaar G J M and Pitchford L C 2005 *Plasma Sources Sci. Technol.* **14** 722

[14] Bazelyan E M and Razhanski I M 1988 *Spark Discharge in Air* (Novosibirsk: Nauka) p. 165

[15] Yuan X H and Raja L L 2003 *IEEE Trans. Plasma Sci.* **31** 495

[16] Neufeld P D, Janzen A R and Aziz R A 1972 *J. Chem. Phys.* **57** 1100

[17] Bird R B, Stewart W E and Lightfoot E N 1960 *Transport Phenomena* (New York: Wiley) p. 46

[18] Farouk T, Farouk B, Gutsol A and Fridman A 2008 *Plasma Sources Sci. Technol.* **17** 035015

[19] Antao D S, Staack D A, Fridman A and Farouk B 2009 *Plasma Sources Sci. Technol* **18** 035016

[20] Staack D, Farouk B, Gutsol A and Fridman A 2005 *Plasma Sources Sci. Technol.* **14** 700

[21] Marode E, Bastien F and Bakker MA 1979 *J. Appl. Phys.* **50** 140

[22] Hagelaar G J M and Pitchford L C 2005 *Plasma Sources Sci. Technol.* **14** 722

[23] Fridman A 2008 *Plasma Chemistry* (Cambridge: Cambridge University Press) p. 146

[24] Sigmond R S 1984 *J. Appl. Phys.* **56** 1355

[25] Wang Q, Economou D J and Donnelly V M 2006 *J. Appl. Phys.* **100** 023

[26] Choi J, Iza F, Lee J K and Ryu C M 2007 *IEEE Trans. Plasma Sci.* **35** 1274

[27] Arkhipenko V I, Zgirovskii S M, Kirillov A A and Simonchick L V 2002 *Plasma Phys. Rep.* **28** 858

[28] Chapman B 1981 *Glow Discharge Processes*: *Sputtering and Plasma Etching* (New York: Wiley) p. 146